Since January 2020 Elsevier has created a COVID-19 resource centre with free information in English and Mandarin on the novel coronavirus COVID-19. The COVID-19 resource centre is hosted on Elsevier Connect, the company's public news and information website.

Biomedical Signal Processing and Control 77 (2022) 103772

Contents lists available at ScienceDirect

Biomedical Signal Processing and Control

journal homepage: www.elsevier.com/locate/bspc

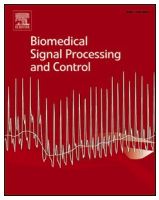

Classification and detection of COVID-19 X-Ray images based on DenseNet and VGG16 feature fusion

Lingzhi Kong, Jinyong Cheng *

School of Computer Science and Technology, Qilu University of Technology (Shandong Academy of Sciences), Jinan 250000, China

ARTICLE INFO

Keywords:
COVID-19
Feature Fusion
DenseNet
VGG16
Image classification

ABSTRACT

Since December 2019, the novel coronavirus disease (COVID-19) caused by the syndrome coronavirus 2 (SARS-CoV-2) strain has spread widely around the world and has become a serious global public health problem. For this high-speed infectious disease, the application of X-ray to chest diagnosis plays a key role. In this study, we propose a chest X-ray image classification method based on feature fusion of a dense convolutional network (DenseNet) and a visual geometry group network (VGG16). This paper adds an attention mechanism (global attention machine block and category attention block) to the model to extract deep features. A residual network (ResNet) is used to segment effective image information to quickly achieve accurate classification. The average accuracy of our model in detecting binary classification can reach 98.0%. The average accuracy for three category classification can reach 97.3%. The experimental results show that the proposed model has good results in this work. Therefore, the use of deep learning and feature fusion technology in the classification of chest X-ray images can become an auxiliary tool for clinicians and radiologists.

1. Introduction

Pneumonia-type illnesses are more contagious during the flu season [1,2]. Chest X-rays (CXRs) play an important role in patient care. Radiologists can use CXR features to determine the type of pneumonia and the underlying pathogenesis [3]. X-ray is one of the most common radiological examination methods for screening and diagnosing chest diseases, as well as the main means of classifying and screening pneumonia, tuberculosis and breast cancer, and is a painless and noninvasive examination method suitable for high populations with relatively low costs [4].

The pandemic of global concern caused by COVID-19 has also brought enormous challenges to governments and the healthcare industry [5-7]. The outbreak was declared a Public Health Emergency of International Concern on 30 January 2020. It was named COVID-19 by the World Health Organization (WHO) in February 2020; around March 2020, the World Health Organization announced that the disease has affected the whole world and is a global pandemic disease [8,9]. The characteristics of COVID-19 are diverse and unpredictable. The common clinical symptoms are mainly respiratory symptoms, and some patients may have gastrointestinal symptoms [10,11]. Real-time polymerase chain reaction (RT–PCR), loop-mediated isothermal amplification (LAMP), antigen testing and other methods can be used to detect COVID-19. Although the specificity of RT–PCR is sufficiently high for COVID-19, its sensitivity is relatively low in detecting COVID-19 [6,12]. LAMP technology has high sensitivity, fast reaction rate and strong specificity, but the design of primers is very complicated, and it is easy to produce nonspecific amplification [13]. Although the antigen test has a relatively fast detection speed, its sensitivity is poor.

Therefore, CXR, as a sensitive method to detect COVID-19 as well as other chest problems, plays an integral role in the early diagnosis and treatment of the disease [12,14]. Previous studies have shown that CXR images have specific differences in the imaging manifestations of common pneumonia and COVID-19. These differences or subtle features can be detected by artificial intelligence. For example, as shown in Fig. 1 [21], it can assist doctors in achieving more accurate classification and diagnosis.

In this study, we reviewed the relevant literature and work on CXR classification. At the same time, artificial intelligence methods were used to efficiently and quickly identify different cases of common pneumonia and COVID-19 as well as to distinguish healthy patients. Therefore, helping doctors to distinguish more accurately among ordinary pneumonia, COVID-19, and healthy patients could lead to more targeted treatment for patients and reduce the duration of illness.

* Corresponding author.
E-mail address: cjy@qlu.edu.cn (J. Cheng).

https://doi.org/10.1016/j.bspc.2022.103772
Received 2 January 2022; Received in revised form 22 April 2022; Accepted 27 April 2022
Available online 8 May 2022

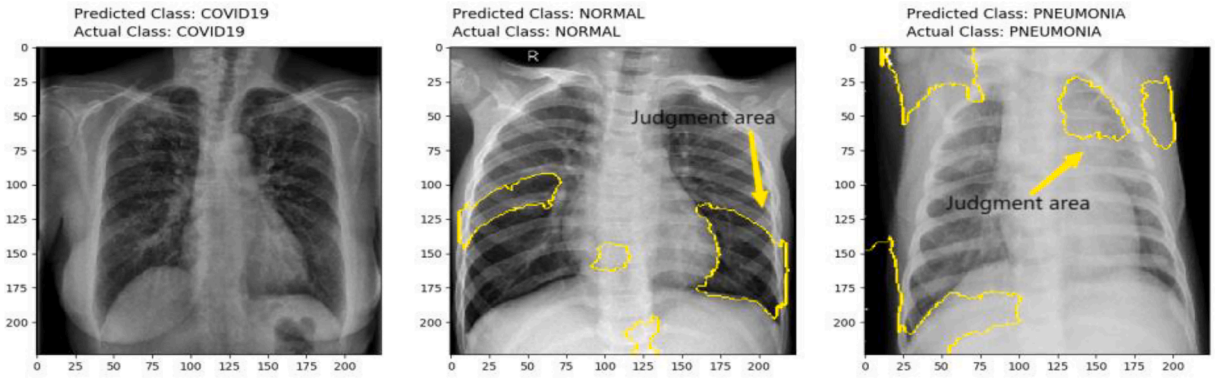

Fig. 1. Detection of chest X-ray image features by artificial intelligence.

The following is the main contribution and summary of the work:

- Prior to this work, an image preprocessing method was applied to CXR data, and segmented images were selected to be sent into the model for more accurate and effective data analysis.
- In this work, we introduced the fine-tuned global attention block (GAB) and category attention block (CAB) for the imbalance of data and distribution to obtain more detailed information of small lesions.
- We fused the DenseNet and VGG models and fine-tuned the model to better detect different pneumonia diseases with convenience, speed and precision.
- We conducted two-category work for healthy and pneumonia patients and three-category work for healthy, common pneumonia, and COVID-19 patients. Compared with other advanced methods, the results show that our model can classify chest X-ray data with high accuracy.

Therefore, in this work, we propose a method based on feature fusion that can more accurately distinguish among healthy, common pneumonia, and COVID-19 patients using chest X-ray images. The main structure of the paper is as follows: Section II discusses the advanced work on using X-ray images for COVID-19. Section III shows data preprocessing of the datasets applied in the work. Section IV provides an in-depth exploration of the fusion models and experiments. Section V obtains and analyzes the experimental results. Artificial intelligence methods were used for the efficient and rapid identification of different cases of general pneumonia and COVID-19 as well as for healthy patients. Section VI analyzes the limitations of this work. Section VII discusses the research topic and prepares for future work.

2. Related work

In recent years, the development of artificial intelligence has been effective in a range of medical fields. The use in healthcare is also on the rise, particularly in medical imaging [15]. Radiological imaging technology, such as chest X-ray scans, can protect patients more effectively, isolate infected patients in time, and distinguish pneumonia types more accurately. A. Narin et al. [16] applied five convolutional neural network models (ResNet50, ResNet101, ResNet152, InceptionV3 and Inception-ResNetV2) to detect patients infected with coronavirus pneumonia using chest X-rays. M. Turkoglu [17] used transfer to learn the features of the convolutional and fully connected layers of the AlexNet model. The SVM classifier was used to detect and classify the important features identified by Relief. The VGG16 pretraining model combined with data enhancement and patching (RICAP) was used to improve robustness and assess the healthy population and COVID-19 [18]. Khan et al. [19] proposed the application of the CoroNet deep convolutional neural network model for automatic chest X-ray detection. Moreover, COVID-19, pneumonia and healthy patients were also classified into three categories, and the classification accuracy of the proposed model was 95%, which greatly promoted the detection of chest diseases. Ouchicha et al. [20] proposed the deep convolutional neural network (CNN) model of CVDNet, which uses chest X-ray images to classify COVID-19 infection from normal and other cases of pneumonia. The architecture is based on a residual neural network, employing two parallel layers of different convolution kernel sizes to capture the local and global features of the input. Through the study and research of the above methods, it was found that although the accuracy of the classification was more accurate in the process of binary classification (healthy population vs. common pneumonia patients, normal vs. COVID-19 patients, and common pneumonia patients vs. COVID-19 patients), in the process of three category classification (healthy, common pneumonia, and COVID-19 patients), the accuracy is generally low, and the three categories cannot be more accurately classified.

3. Dataset

3.1. Dataset

This study used two different publicly available datasets to collect chest X-ray images to create one dataset. The dataset contains a total of 6518 images, and the test set data account for 20% of the total data. The first is from a publicly available dataset. Chest X-ray images (before and after) were selected from pediatric patients aged 1 to 5 years at the Guangzhou Women's and Children's Medical Center [21]. All chest X-ray imaging was performed as part of the patient's routine clinical care. To analyze chest X-ray images, all chest X-ray images were screened for quality control by removing all low-quality or unreadable scans. The second dataset is the COVID-19 X-ray image database developed by Joseph et al. [22], which utilizes images from various open access sources. The authors collected images relevant to radiology from various authentic sources (Radiology Society of North America (RSNA), Encyclopedia of Radiology, etc.). Most research on COVID-19 has used images from this source. The repository contains an open database of COVID-19 cases with chest X-ray images and is being updated regularly.

3.2. Data preprocessing

Low-dose X-ray images suffer from blurred edges, low contrast due to objective factors, and a low signal-to-noise ratio of projections. To better extract chest X-ray image features, image segmentation technology was used to remove the background noise and retain only the effective chest shadow area. In the course of our experimental study, data enhancement techniques were applied to enrich medical image datasets. In the images of the datasets used in this study, the size, shape, shadow area and location of the chest lesions precisely varied from patient to patient.

(1) All images in the training set were traversed, and the "inference" function was called. ResNet34 [23] was used for semantic segmentation

Fig. 2. Stepwise segmentation of chest X-ray images by ResNet34 (X-ray image, recognition of the chest region image, and chest image after removing the background).

Table 1
Distribution of different types of data in the dataset.

Labels	Train (80%)	Test (20%)	Total (100%)
COVID-19	460	116	576
HEALTHY	1266	317	1583
PNEUMONIA	3418	855	4273
Total	5230	1288	6518

learning, and the segmentation threshold was set to 0.2.

(2) Images of different sizes were scaled to 512 × 512. The mask area marked with red and green was returned.

(3) The original image data value was converted into a 255-level gray value image by enhancing the information of the lung shadow area and surrounding tissues.

(4) Finally, the effective region was segmented by the dot product of the grayscale image and the mask data matrix. The redundant parts were removed, and chest X-ray images without background were obtained.

Therefore, we created a new chest X-ray image dataset: the chest X-ray images were horizontally flipped, and 3x3 Gaussian blur was added to reduce the overfitting of the model during training and effectively achieve the invariant stability of the model learning process. The segmented images not only have the noise redundant background regions removed but also help the model to accurately analyze images of healthy, common pneumonia, and COVID-19 patients. Fig. 2 shows the step-by-step segmentation of normal subject chest X-ray images (X-ray image, recognition of the chest region image, and chest image after removing the background).

We unified the segmented images in the form of.jpg and classified them by type. Eighty percent of the data were used for training, and the remaining 20% were used for testing. That is, the total amount of data in the training set was 5230, and the total amount of data in the test set was 1288. The specific situation of the chest X-ray dataset prepared by us is presented in Table 1.

4. Method

4.1. Model connection and feature fusion

4.1.1. DenseNet

For our first piece of model, we use a 201-layer dense connected

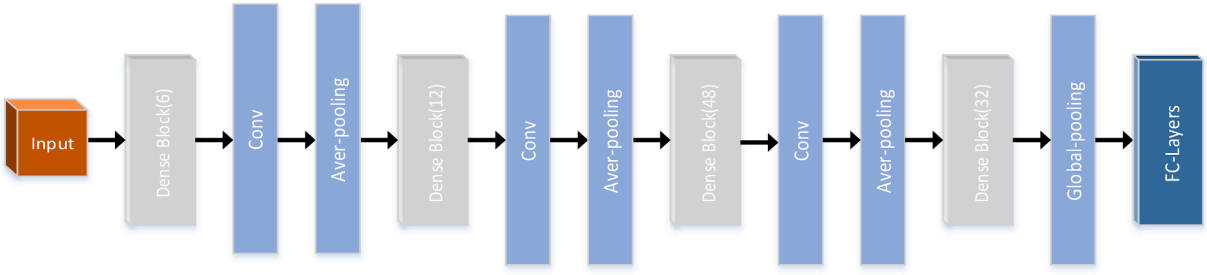

Fig. 3. Structure diagram of the DenseNet201 model.

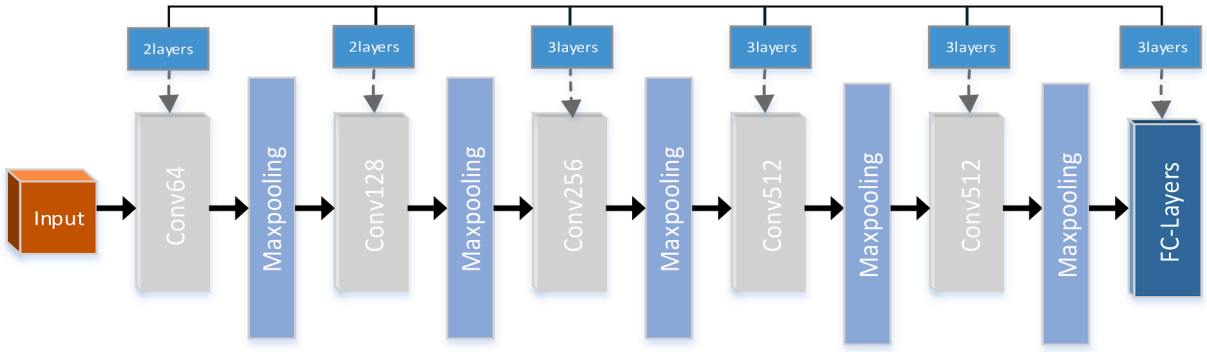

Fig. 4. VGG16 model structure diagram.

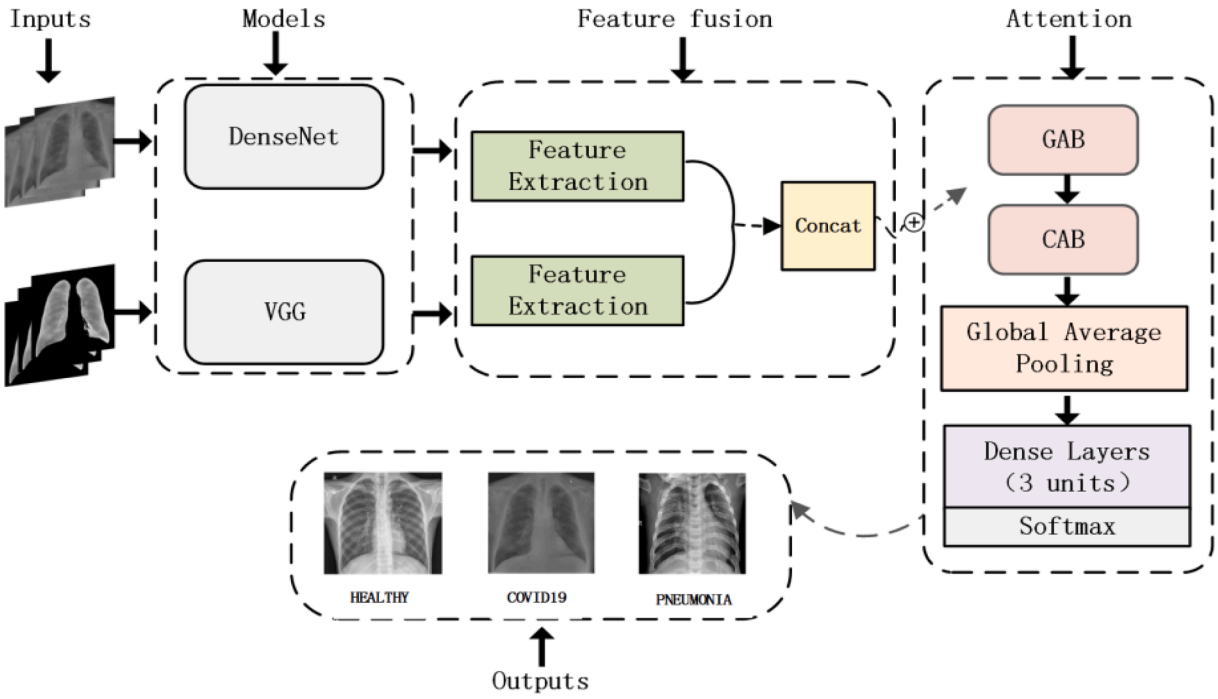

Fig. 5. Model fusion network diagram after segmentation and addition of the attention mechanism.

convolutional network (DenseNet). As shown in Fig. 3, the network layer of DenseNet201 is densely linked by four network blocks, and the dense blocks are uniformly connected by transition layer pooling. Finally, the feature map of the last layer is pooled by global average pooling to form a feature point. These feature points constitute the final feature vector, which is calculated in SoftMax [24]. The DenseNet model mainly realizes feature reuse through feature connection on the channel. There are two basic methods in feature reuse: bypass and concatenation. Since gradient disappearance usually occurs in the deep layer of the network, it is more appropriate to place bypass layers at the beginning of the deep layer of the network [25]. The dense connection mechanism is that each layer will be connected with all the previous layers on the channel dimension as input to the next layer. It is more efficient to achieve feature reuse. In the traditional network, the output of the l layer is represented as, $x_l = H_l(x_{l-1})$ while in DenseNet, all layer dense connection modes are represented as$x_l = H_l([x_0,x_1,\ldots,x_{l-1}])$. $H_l(\cdot)$ stands for nonlinear transformation. The structure of Batchnorm + ReLU + 3 × 3Conv can be used to obtain more input features and improve the efficiency of feature reuse. It not only greatly reduces the number of network parameters but also alleviates the vanishing gradient problem to a certain extent [26].

4.1.2. Vgg16

The second model used in this work is the VGG network structure. The VGG16 network can not only increase the network depth but also improve the performance more effectively. The simple module is composed of a small convolution kernel, small pooling kernel and ReLU. As shown in Fig. 4, there are 5 convolutional layers, 3 fully connected layers and a softmax output layer. Max pooling is used to separate the layers, and the ReLU function is used for the activation units of all hidden layers [27]. Therefore, one of the great advantages of VGG networks is that they simplify the structure of neural networks. The obtained 7 × 7 × 512 feature map is fully connected, and then softmax activation is carried out to output the recognition results of the three objects.

4.1.3. Model fusion

Since we have adopted datasets of different scales and styles in our work, we use different network models to extract and identify their application performance. Therefore, to achieve the best quality model classification, we used the methods of model connection [28] and feature fusion [29] to build the model in this study, which are mainly applied to the two network structures. DenseNet and VGG16 have a clear division of labor. Using the characteristics of the two networks, corresponding adjustments are made in the input of the dataset. The original image is first fed into the DenseNet network model architecture, which slows down the vanishing gradient problem and enhances feature propagation [30]. Then, the dataset generated by ResNet34 is sent to the VGG16 network model. Increasing the network depth affects the final performance of the network to a certain extent. The mobility is enhanced while reducing the error rate, and the generalization to other image data is also good [31]. Finally, ensemble learning is used to fuse the features, and two attention mechanisms (global attention block and category attention block) are used to solve the problem of the weak generalization ability of a single neural network, as shown in Fig. 5.

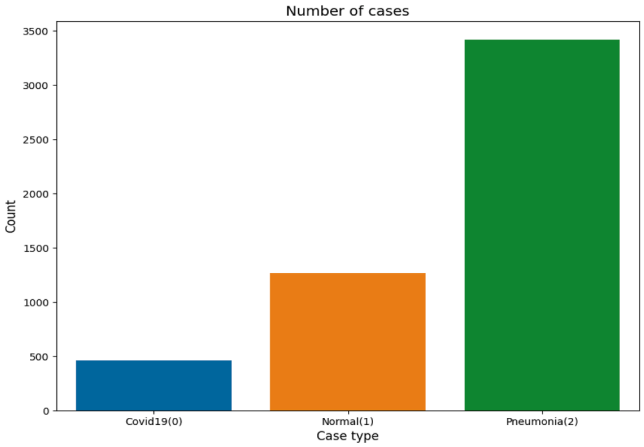

Fig. 6. Distribution of imbalanced datasets.

4.2. Sample balance and attention mechanism addition

From Fig. 6, we can clearly find that there is a serious imbalance in the proportion of images obtained in different datasets, which can easily lead to problems such as a decline in the predictive ability of the model and a large error [32]. In response to the imbalance of data samples, two main parts are added to the work to equalize the data samples: (1) the "class_weight" function in the Keras library and (2) the attention mechanism.

4.2.1. Sample balance

Using the class_weight function in the Keras library changes the range of loss, which may affect the stability of training [33]. We can choose "balanced" to let the library automatically increase the weight of illegal user samples. "Balanced" improves the weight of certain categories so that more sample categories will be classified into high-weight categories than without considering the weight, thus balancing the number of samples in the dataset. The weight calculation formula under "balanced" can be expressed as:

$$W_i = Sum/(Class \times Sum_i) \tag{1}$$

W_i indicates the final calculated weight value of each category, and i represents the number of 3 categories. *Sum* represents the size of all samples in this type of dataset. *Class* represents the number of categories in the total sample. Sum_i indicates the number of samples corresponding to class*i*.

4.2.2. Attention mechanism

For the problems in Fig. 6, the uneven distribution of COVID-19, healthy, and pneumonia data leads to a high level of concern in the model. The sample imbalance greatly affects the performance of the final classification. As mentioned in the literature [34], CBAM is a lightweight general module that can be better applied to any CNN architecture and has a small sales volume, thus playing a significant role in the application of GAB and CAB [35]. GAB can be used to preserve detailed pathological information in pneumonia images and suppress color features and brightness features of similar parts. CAB can be used to learn distinguishing features to better solve the problem of low accuracy caused by an uneven distribution of data.

In Eq. (2), Z_{ch_at} is used to calculate the attention feature of the channel, where H represents the height, W represents the width, and C represents the number of channels. δ means using the sigmoid activation function, *GAP* means average pooling, and Z_{G-IN} uses a 1×1 convolution to reduce the number of channels.

$$Z_{ch\_at} = (\delta(Conv2(GAP(Z_{G-IN})))) \otimes Z_{G-IN} Z \in R^{H\times W\times C} Z_{G-IN} \in R^{H\times W\times C'} C' = C/2 \tag{2}$$

C_G stands for cross-channel average pooling and saves more detailed information about small lesions in Eq. (3). Different lesions in chest X-ray images can be better divided into details as input of*CAB*. The number of channels required by Z' to detect each category discrimination area is obtained. Z'' retains half of the features. The dropout function is removed, and all the features are predicted.

$$Z_{G-OUT} = Z_{ch\_at} \otimes (\delta(C\_G(Z_{ch\_at}))) \tag{3}$$

The representative in Eq. (4) responds to the importance of each category feature map. *GMP* stands for global max pooling. By averaging the sum of Z'' pooling, the score $S = \{S_1, S_2, ...S_L\}$ of each category is calculated.

$$S_i = \frac{1}{m}\sum_{j=1}^{m} GMP(z''_{ij}) i \in \{1,2,3,...,L\} S = \{S_1, S_2, ...S_L\} \tag{4}$$

Z_{i_avg} in Eq. (5) represents the mapping response of the semantic features of the i-th class. z'_{ij} represents the response of the j-th feature of the i-th class inZ'. The calculated scores for each class are multiplied, summed, and averaged by the semantic features of that class to obtainA_{CAB}, which provides the area of diagnosis, as shown in Eq. (6). Finally, Z_{G-IN} can be transformed into feature map Z_{c-out} through the category attention mechanism. We can obtain the classification situation after sample equilibrium more accurately. Compared with the balanced sample, the efficiency is up to 97.3%.

$$Z'_{i\_avg} = \frac{1}{m}\sum_{j=1}^{m} z'_{ij} i \in \{1,2,3,...,L\} \tag{5}$$

$$A_{CAB} = \frac{1}{L}\sum_{i=1}^{L} S_i Z'_{i\_avg} A_{CAB} \in R^{H\times W\times 1} \tag{6}$$

$$Z_{C-OUT} = Z_{C-IN} \otimes A_{CAB} \tag{7}$$

4.3. Setting hyperparameters

In this paper, the hyperparameters of the model are tuned, and much work is mainly done on the batch size (Batch_size), optimizer (Optimizer), loss function (Loss), and normalization operation (BN). The best results of the work comparison are provided in Table 2. Although the sample of the initial dataset was unbalanced, the optimizer combined with Adam was faster and more efficient than other optimizers with the application of class_weight and the adjustment of the attention mechanism [36]. The Adam optimizer has the highest accuracy and plays an indispensable role in other deep learning algorithms in the medical field [37]. The difference between the probability distribution trained by the cross entropy loss function (categorical_crossentropy) [38] and the true distribution is obtained. It describes the distance between the actual output (probability) and the expected output (probability); that is, the smaller the cross entropy value is, the closer the two probability distributions will be [39], as shown in Eq. (8). At the same time, the Label_smoothing function is used to set the parameter "Label_smoothing" to smooth the label. It increases the generalization ability of the model and prevents overfitting to some extent.

$$loss = -\sum_{i=1}^{n} \widehat{y}_{i1} log y_{i1} + \widehat{y}_{i2} log y_{i2} + ... + \widehat{y}_{im} log y_{im} \tag{8}$$

$$\frac{\delta loss}{\delta y_{i1}} = -\sum_{i=1}^{n} \frac{\widehat{y}_{i1}}{y_{i1}}$$

$$\frac{\delta loss}{\delta y_{i2}} = -\sum_{i=1}^{n} \frac{\widehat{y}_{i2}}{y_{i2}} \tag{9}$$

$$\frac{\delta loss}{\delta y_{im}} = -\sum_{i=1}^{n} \frac{\widehat{y}_{im}}{y_{im}}$$

n represents the number of samples, m represents the number of classifications, $\widehat{y}$ represents the true label of the original image, and y represents the predicted label. Since loss is a multioutput function, the calculation of loss is also a multiple process. For example, Eq. (9) is affected by the error, so when the error is large, the weight updates quickly, while when the error is small, the weight updates slowly.

Table 2
Optimal hyperparameter values.

Hyperparameter	Value
Batch_size	16
Optimizer	Adam
Learning_rate	0.0001
Loss	categorical_crossentropy
Epochs	80

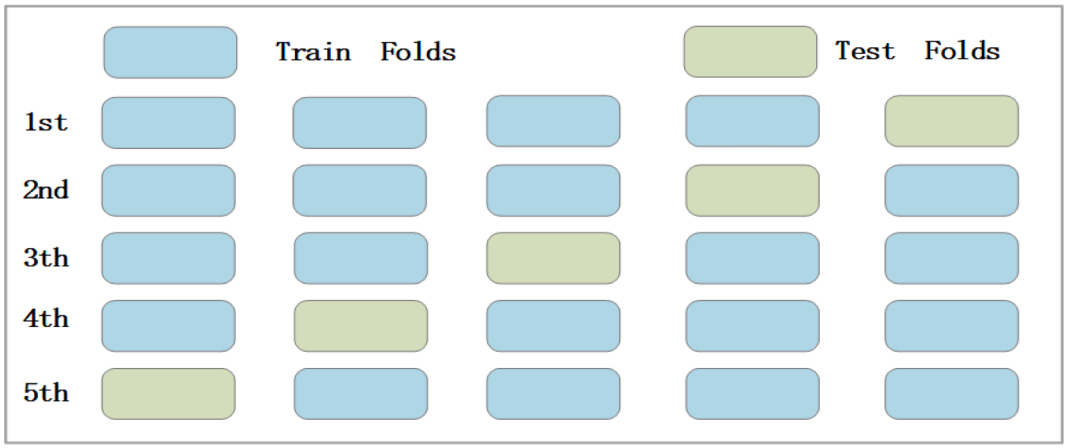

Fig. 7. Fivefold cross-validation renderings.

Table 3
Accuracy and loss values after fivefold cross-validation (two classifications).

Folds	Accuracy	Loss	RMSE	Precision	Recall	F1-score
Fold1	0.980	0.074	0.171	0.939	0.984	0.962
Fold2	0.970	0.151	0.169	0.920	0.956	0.938
Fold3	0.977	0.123	0.170	0.922	0.965	0.935
Fold4	0.979	0.094	0.173	0.952	0.965	0.959
Fold5	0.988	0.056	0.166	0.923	0.985	0.954
Average	0.979	0.100	0.169	0.931	0.971	0.950

Table 4
Accuracy and loss values after fivefold cross-validation (three category classification).

Folds	Accuracy	Loss	RMSE	Precision	Recall	F1-score
Fold1	0.978	0.218	0.193	0.954	0.932	0.942
Fold2	0.968	0.276	0.219	0.928	0.952	0.937
Fold3	0.974	0.185	0.204	0.971	0.933	0.952
Fold4	0.967	0.123	0.213	0.941	0.966	0.953
Fold5	0.979	0.195	0.192	0.982	0.956	0.969
Average	0.973	0.199	0.204	0.955	0.948	0.951

5. Work results and analysis

5.1. Fivefold Cross-validation

To effectively adjust the volatility and stability of the detection results, the model in this paper adopts the k-fold cross-validation method. We randomly divided the dataset into m equal parts, which gives$D_1, \ldots, D_m$. For example,

$$\bigcup_{i=1}^{m} D_i = D_{dataset} \forall 1 \leqslant i \leqslant m | D_i | \approx \frac{|D_{dataset}|}{m} \forall 1 \leqslant i \leqslant m \tag{10}$$

In this work, we set m = 5 and perform the following steps:

Step 1: Divide the data sample into 5 equal parts.

Step 2: Take one copy of each work for testing, and use the rest for training.

Step 3: Average five times.

As shown in Fig. 7, for the first time, the work takes the first copy as the test set and the rest as the training set. For the second time, the work takes the second copy as the test set and the rest as the training set. The result is averaged by Eq. (11).

$$Accuracy_{test} = \frac{1}{m} \sum_{i=1}^{m} Accuracy_i \tag{11}$$

From Table 3 and Table 4, the work of fivefold cross-validation is carried out for two classes and three classes, respectively. Finally, the performance indicators (precision, recall and F1-score) are considered, and the classified reports are given. The overall performance is obtained by averaging each fold. Through the corresponding confusion matrices in Figs. 11 and 12, the classification performance can be analyzed better.

Table 5
Comparison of ablation experiments.

Model	Accuracy	Precision	Recall	F1-score
DenseNet	0.943	0.942	0.957	0.948
VGG16	0.931	0.946	0.946	0.946
DenseNet + VGG16	0.964	0.943	0.949	0.946
DenseNet + GAB + CAB	0.953	0.948	0.954	0.951
VGG16 + GAB + CAB	0.951	0.949	0.950	0.949
Our Model	0.973	0.948	0.951	0.955

5.2. Ablation experiment

To evaluate the effectiveness of model fusion with the addition of an attention mechanism, we conducted additional ablation experiments on chest X-ray, as shown in Table 5. The work application model is mainly composed of DenseNet and VGG16. One component is deleted at a time, including model actions, attention actions, and fusion actions. First, the attention mechanism is removed, and the accuracy, precision, recall and F1-score under a single model are calculated separately. The accuracy index decreased by approximately 0.04 at most, and other evaluation criteria also declined. Second, the overall performance of the two models is slightly improved by combining the relevant features. The accuracy increased by approximately 0.03. Finally, the attention mechanism is added to the basic model, and the overall index rises by approximately 0.01, indicating that the attention module plays an important role in enhancing relevant features. Therefore, the proposed feature fusion model can improve the efficiency of chest X-ray image classification to a certain extent.

5.3. Comparison of work effects

In this paper, the work environment carried out research and discussion on multiple classifications of two different datasets: healthy vs. pneumonia-type patients and healthy vs. pneumonia vs. COVID-19 patients.

5.3.1. Work analysis of HEALTHY patients and patients with pneumonia (Two Categories)

Chest X-ray images were used to distinguish the work of healthy patients from those of pneumonia patients (bacterial, viral, and COVID-

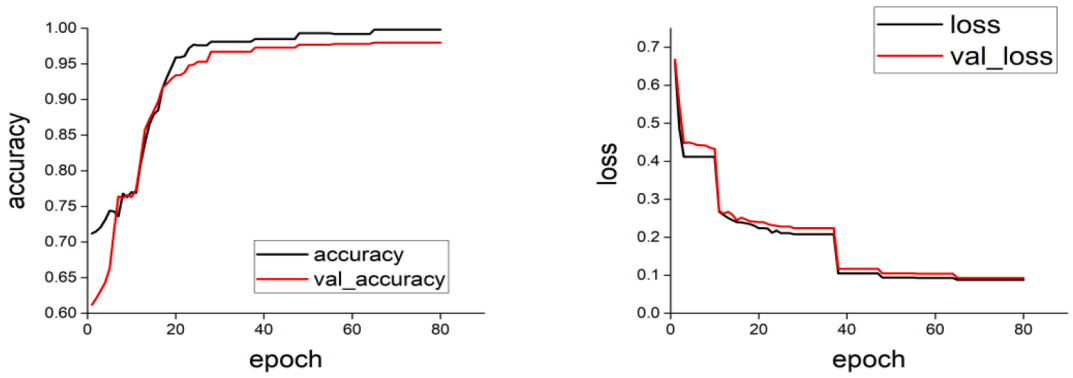

Fig. 8. (a): Comparison of accuracy and val_accuracy in binary classification (HEALTHY vs. PNEUMONIA); (b): Comparison of loss and val_loss in two classifications (HEALTHY vs. PNEUMONIA).

Table 6
Binary classification (HEALTHY vs. PENUMONIA) results under different advanced models.

Reference	Type	Dataset	Result (Accuracy)
[40]	HEALTHY vs. PENUMONIA	5856 images (CXR)	93.01%
[41]	HEALTHY vs. PENUMONIA	453 images (CXR)	73.10%
[42]	HEALTHY vs. PENUMONIA	618 images (CXR)	86.7%
[43]	HEALTHY vs. PENUMONIA	5856 images (CXR)	96.2%
Our Model	HEALTHY vs. PENUMONIA	6518 images (CXR)	97.9%

Table 7
Work results on the same dataset under different advanced models.

Reference	Accuracy	Precision	Recall	F1-score
[44]	0.940	0.970	0.930	0.950
[45]	0.930	0.870	0.970	–
[46]	0.950	–	–	–
Our Model	0.979	0.95	0.96	0.96

19). From Fig. 8(a)(b), we can clearly see that 80 iterations can make the accuracy stable. In the first 20 iterations, the growth rate of accuracy increased significantly, and then the growth rate gradually showed a slow upward trend. In comparison with other advanced models, work in this field has achieved good results, as shown in Table 6. The results in Table 7 show that the accuracy effect calculated by this work model is relatively successful. The confusion matrix in Fig. 11 clearly shows the classification effect of the binary classification. In addition, it also has a relatively high result in other evaluation indicators, and the model has obvious advantages in classification.

5.3.2. Work analysis of Healthy, common pneumonia and COVID-19 patients (Three Categories)

To verify the generalization ability of the model, we also conducted research on the three categories of healthy, common pneumonia and

Table 8
Results of three category classification (HEALTHY vs. PENUMONIA vs. COVID-19) under different models.

Reference	Type	Dataset	C-Result (Accuracy)
[47]	HEALTHY vs. PENUMONIA vs. COVID-19	171 COVID19, 60 PNEUMONIA, 76 HEALTHY	90.82%
[48]	HEALTHY vs. PENUMONIA vs. COVID-19	434 COVID19, 1100 PNEUMONIA, 1100 HEALTHY	94.1%
[49]	HEALTHY vs. PENUMONIA vs. Influenza-A	219 COVID19 (CT), 224 Influenza-A, 175 HEALTHY	86.7%
[14]	HEALTHY vs. PENUMONIA vs. COVID-19	53 COVID19 (+), 5526 COVID19 (-), 8066 HEALTHY	92.4%
Our Model	HEALTHY vs. PENUMONIA vs. COVID-19	576 COVID19, 4273 PNEUMONIA, 1583 HEALTHY	97.3%

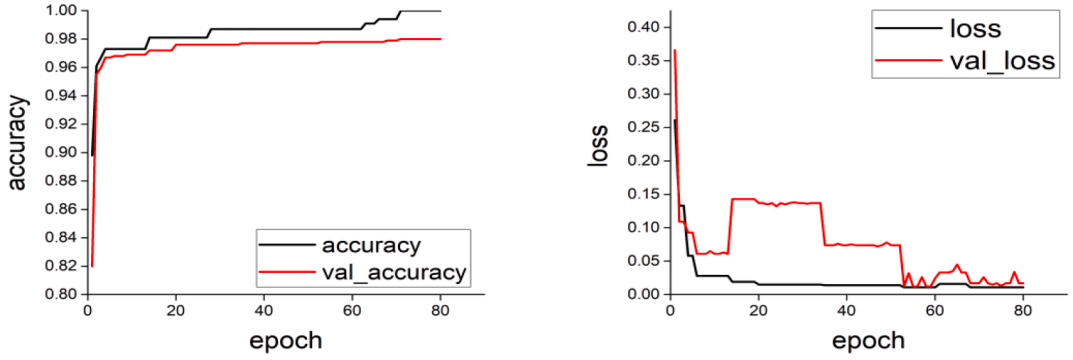

Fig. 9. (a): Comparison of accuracy and val_accuracy in three categories (HEALTHY vs. PNEUMONIA vs. COVID-19); (b): Comparison of loss and val_loss in three categories (HEALTHY vs. PNEUMONIA vs. COVID-19).

Table 9
Comparison of similar datasets under different models.

Reference	Accuracy	Precision	Recall	F1-score
[50]	0.910	0.920	0.870	0.880
[51]	0.940	0.913	–	–
[19]	0.95	0.950	0.969	0.956
Our Model	0.973	0.955	0.948	0.951

COVID-19 patients. Different forms of datasets are input for different models, and detailed segmentation is used to better optimize the X-ray images of the chests and extract key features. From the work results in Fig. 9(a)(b), the fit of the training data and the test data curve is good. During the first 15 iterations, the overall upward trend was faster. We also compare this field with other advanced models, as shown in Table 8. The accuracy can reach 97.3%.

Similar datasets are compared in Table 9. The accuracy of the evaluation index is generally stable and high. Compared with the recall data in Ref. [19], the value is relatively low, but the average value among other data is relatively stable and above 0.95. According to the model commonly used in medical images, a comparison is made. Fig. 10 and Table 10 show the comparison of accuracy, loss and time consumption of different models on the same dataset. Under different models, our model training and test sets have the highest accuracy and the lowest loss. Although slightly longer in time consumption, the overall performance is the best. The confusion matrix in Fig. 12 clearly shows the classification effect of the three category classification.

As shown in Fig. 13(a)(b), the ROC distribution diagram also shows that the accuracy of the ROC in the second classification is as high as 99%, and the accuracy of different diseases in the third classification fluctuates at 99%. It can also be better explained that the higher the index is, the higher the accuracy of the model diagnosis.

6. Limitations

Due to the limited number of COVID-19 datasets now available for public research applications, the sources for obtaining COVID-19 images are constantly updated. The research object of the work is relatively limited. Two publicly available datasets were used in this study. How to

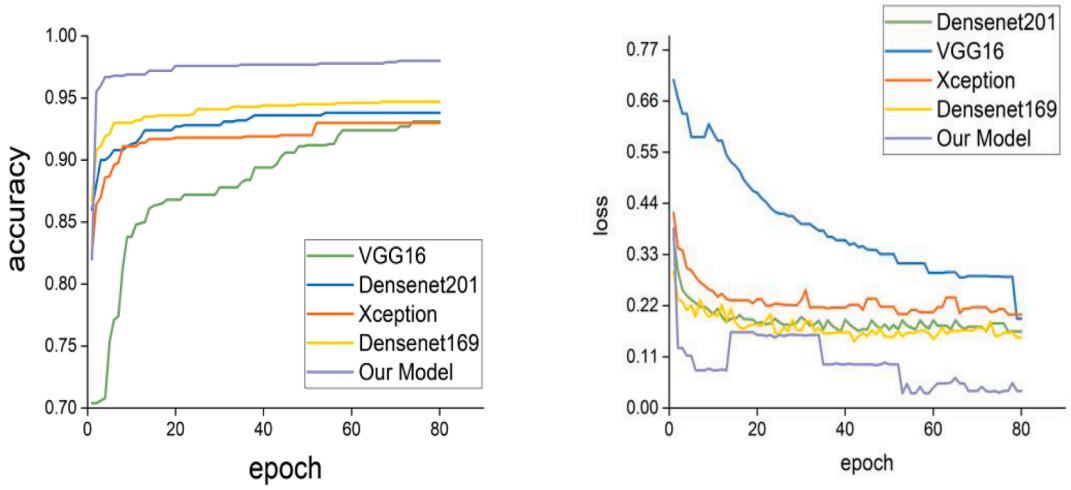

Fig. 10. (a): Comparison of accuracy and val_accuracy of different models under the same dataset; (b): Comparison of loss and val_loss of different models under the same dataset.

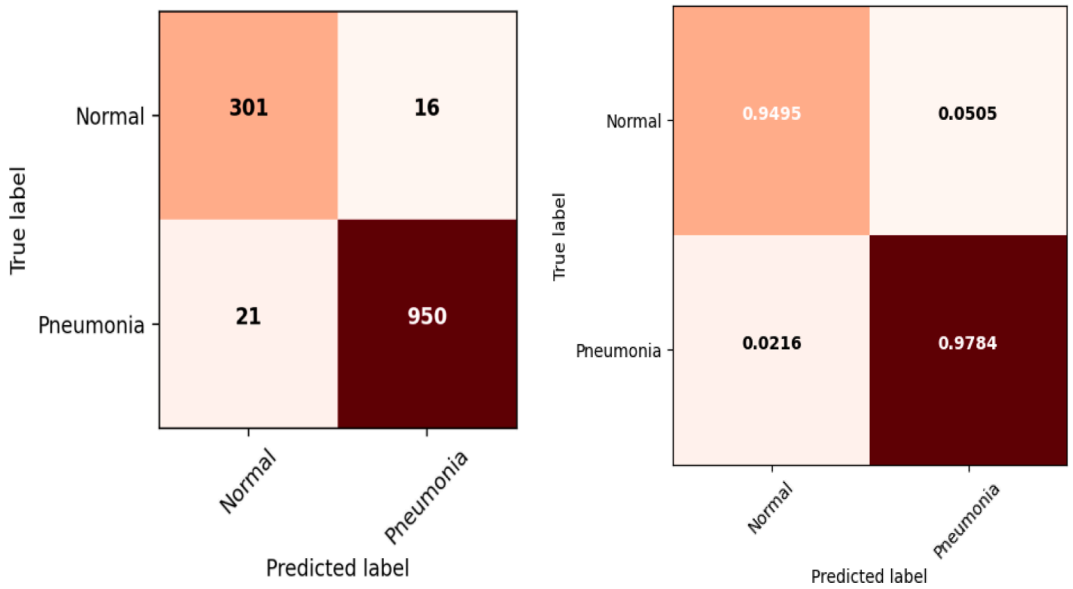

Fig. 11. (a): Confusion matrix for binary classification (HEALTHY vs. PNEUMONIA vs. COVID-19); (b): Confusion matrix (percentage) for binary classification (HEALTHY vs. PNEUMONIA vs. COVID-19).

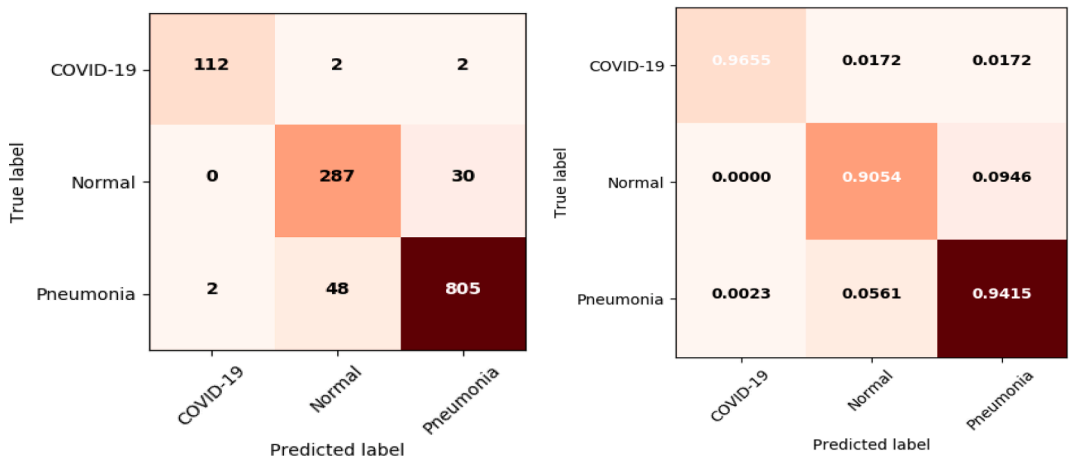

Fig. 12. (a): Confusion matrix for three categories (HEALTHY vs. PNEUMONIA vs. COVID-19); (b): Confusion matrix (percentage) for three categories (HEALTHY vs. PNEUMONIA vs. COVID-19).

Table 10
Comparison of different models under the same dataset.

Datasets	Models	Train_acc	Test_acc	Train_loss	Test_loss	Time
Three classes (X-ray)	DenseNet201	0.965	0.938	0.104	0.165	104 min
	VGG16	0.987	0.891	0.294	0.281	90 min
	DenseNet169	0.962	0.947	0.109	0.144	103 min
	Xception	0.944	0.930	0.167	0.202	100 min
	Our model	0.999	0.973	0.004	0.098	110 min

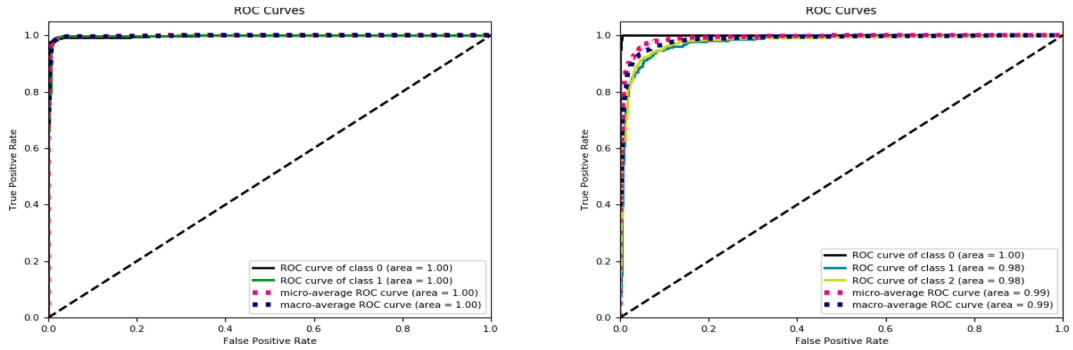

Fig. 13. (a): Distribution of ROC curves for binary classification (HEALTHY vs. PNEUMONIA); (b): Distribution of ROC curves for three categories (HEALTHY vs. PNEUMONIA vs. COVID-19).

better assist doctors in becoming an important part of the clinical work testing process requires more data and image learning and research.

7. Conclusion

At a time when an increasing number of people are infected with COVID-19, using AI methods to create effective and rapid tests will certainly reduce the workload of healthcare workers. In this paper, a feature fusion-based chest X-ray image classification method is proposed. Successful detection of healthy, common pneumonia, and COVID-19 cases from chest images (X-ray) is demonstrated. By using ResNet34 to effectively process the segmentation of the dataset, the extraction of features is more efficient. Based on the fusion of DenseNet and VGG16, GAB and CAB attention blocks can be added to carry out detailed feature extraction of regions. Due to the highly similar X-ray results of COVID-19 and other common pneumonia diseases, doctors may have some misdiagnoses in diagnosis. It is therefore crucial to make a precise distinction between ordinary pneumonia and COVID-19. The work showed that when distinguishing ordinary pneumonia, COVID-19 and healthy patients, the accuracy, precision, recall and F1-score reached 97.3%, 95.5%, 94.8% and 95.1%, respectively. Compared with those with pneumonia, the accuracy, precision, recall and F1-score reached 97.9%, 95.0%, 96.0% and 96.0%, respectively. The model was tested using X-ray images of tuberculosis to see if it had a strong generalization ability [52]. The accuracy, precision, recall and F1-score reached 99%, 99%, 99% and 99%. Despite the positive results, more clinical trials and studies are needed to test this model. Better auxiliary imaging for doctors, improvement of the accuracy of diagnosis, and a more in-depth study of the differences between different pneumonias in a timely manner so that patients could avoid the pain of the disease are needed. Considering the present work, there are still gaps in some research fields, which can be discussed and realized in future work:

1. To better realize clinical applications, it is necessary to expand the number of multiclass datasets so that the model can accurately judge chest X-ray and provide a more accurate classification diagnosis.

2. The proposed model should be further optimized and improved and combined with an SVM classifier to improve the multicategory diagnosis ability.

CRediT authorship contribution statement

Lingzhi Kong: Conceptualization, Methodology, Software, Writing – original draft. **Jinyong Cheng:** Supervision, Validation.

Declaration of Competing Interest

The authors declare that they have no known competing financial interests or personal relationships that could have appeared to influence the work reported in this paper.

References

[1] A. Scohy, A. Anantharajah, M. Bodéus, B. Kabamba-Mukadi, A. Verroken, H. Rodriguez-Villalobos, Low performance of rapid antigen detection test as frontline testing for COVID-19 diagnosis, J. Clin. Virol. 129 (2020) 104455.

[2] M. Nagura-Ikeda, K. Imai, S. Tabata, K. Miyoshi, N. Murahara, T. Mizuno, M. Horiuchi, K. Kato, Y. Imoto, M. Iwata, S. Mimura, T. Ito, K. Tamura, Y. Kato, M. B. Miller, Clinical evaluation of self-collected saliva by quantitative reverse transcription-PCR (RT-qPCR), Direct RT-qPCR, reverse transcription-loop-mediated isothermal amplification, and a rapid antigen test to diagnose COVID-19, J. Clin. Microbiol. 58 (9) (2020), https://doi.org/10.1128/JCM.01438-20.

[3] G. Wang, X. Liu, J. Shen, C. Wang, Z. Li, L. Ye, X. Wu, T. Chen, K. Wang, X. Zhang, Z. Zhou, J. Yang, Y.e. Sang, R. Deng, W. Liang, T. Yu, M. Gao, J. Wang, Z. Yang, H. Cai, G. Lu, L. Zhang, L. Yang, W. Xu, W. Wang, A. Olvera, I. Ziyar, C. Zhang, O. Li, W. Liao, J. Liu, W. Chen, W. Chen, J. Shi, L. Zheng, L. Zhang, Z. Yan, X. Zou, G. Lin, G. Cao, L.L. Lau, L. Mo, Y. Liang, M. Roberts, E. Sala, C.-B. Schönlieb, M. Fok, J.-N. Lau, T. Xu, J. He, K. Zhang, W. Li, T. Lin, A deep-learning pipeline for the diagnosis and discrimination of viral, non-viral and COVID-19 pneumonia from chest X-ray images, Nat. Biomed. Eng. 5 (6) (2021) 509–521.

[4] X. Wang, Y. Peng, L. Lu, Z. Lu, M. Bagheri, R.M. Summers, ChestX-ray8: Hospital-scale chest X-ray database and benchmarks on weakly-supervised classification and localization of common thorax diseases, in, Proc. - 30th IEEE Conf. Comput. Vis. Pattern Recognition, CVPR (2017), https://doi.org/10.1109/CVPR.2017.369.

[5] M.L. Ranney, V. Griffeth, A.K. Jha, Critical supply shortages — the need for ventilators and personal protective equipment during the Covid-19 Pandemic, N. Engl. J. Med. 382 (18) (2020) e41.

[6] J.-W. Chan, S. Yuan, K.-H. Kok, K.-W. To, H. Chu, J. Yang, F. Xing, J. Liu, C.-Y. Yip, R.-S. Poon, H.-W. Tsoi, S.-F. Lo, K.-H. Chan, V.-M. Poon, W.-M. Chan, J.D. Ip, J.-P. Cai, V.-C. Cheng, H. Chen, C.-M. Hui, K.-Y. Yuen, A familial cluster of pneumonia associated with the 2019 novel coronavirus indicating person-to-person transmission: a study of a family cluster, Lancet. 395 (10223) (2020) 514–523.

[7] C. Huang, Y. Wang, X. Li, L. Ren, J. Zhao, Y.i. Hu, L.i. Zhang, G. Fan, J. Xu, X. Gu, Z. Cheng, T. Yu, J. Xia, Y. Wei, W. Wu, X. Xie, W. Yin, H. Li, M. Liu, Y. Xiao, H. Gao, L.I. Guo, J. Xie, G. Wang, R. Jiang, Z. Gao, Q.i. Jin, J. Wang, B. Cao, Clinical features of patients infected with 2019 novel coronavirus in Wuhan, China, Lancet. 395 (10223) (2020) 497–506.

[8] D.S. Hui, E. I Azhar, T.A. Madani, F. Ntoumi, R. Kock, O. Dar, G. Ippolito, T. D. Mchugh, Z.A. Memish, C. Drosten, A. Zumla, E. Petersen, The continuing 2019-nCoV epidemic threat of novel coronaviruses to global health — The latest 2019 novel coronavirus outbreak in Wuhan, China, Int. J. Infect. Dis. 91 (2020) 264–266.

[9] P. Zhou, X.-L. Yang, X.-G. Wang, B. Hu, L. Zhang, W. Zhang, H.-R. Si, Y. Zhu, B. Li, C.-L. Huang, H.-D. Chen, J. Chen, Y. Luo, H. Guo, R.-D. Jiang, M.-Q. Liu, Y. Chen, X.-R. Shen, X.i. Wang, X.-S. Zheng, K. Zhao, Q.-J. Chen, F. Deng, L.-L. Liu, B. Yan, F.-X. Zhan, Y.-Y. Wang, G.-F. Xiao, Z.-L. Shi, A pneumonia outbreak associated with a new coronavirus of probable bat origin, Nature. 579 (7798) (2020) 270–273.

[10] T. Singhal, A Review of Coronavirus Disease-2019 (COVID-19), Indian J. Pediatr. 87 (4) (2020) 281–286.

[11] COVID-19 symptoms https://www.who.int/health-topics/coronavirus#tab=tab_ 3 Last Accessed: 3 Apr 2020.

[12] Y. Fang, H. Zhang, J. Xie, M. Lin, L. Ying, P. Pang, W. Ji, Sensitivity of chest CT for COVID-19: Comparison to RT-PCR, Radiology. 296 (2) (2020) E115–E117.

[13] K. Green, A. Winter, R. Dickinson, S. Graziadio, R. Wolff, S. Mallett, A.J. Allen, What tests could potentially be used for the screening, diagnosis and monitoring of COVID-19 and what are their advantages and disadvantages ? Cent, Evidence-Based Med, 2020.

[14] L. Wang, Z.Q. Lin, A. Wong, COVID-Net: a tailored deep convolutional neural network design for detection of COVID-19 cases from chest X-ray images, Sci. Rep. 10 (1) (2020), https://doi.org/10.1038/s41598-020-76550-z.

[15] C. Dhiman, D.K. Vishwakarma, View-invariant deep architecture for human action recognition using two-stream motion and shape temporal dynamics, IEEE Trans. Image Process. 29 (2020) 3835–3844.

[16] A. Narin, C. Kaya, Z. Pamuk, Automatic detection of coronavirus disease (COVID-19) using X-ray images and deep convolutional neural networks, Pattern Anal. Appl. 24 (3) (2021) 1207–1220.

[17] M. Turkoglu, COVIDetectioNet: COVID-19 diagnosis system based on X-ray images using features selected from pre-learned deep features ensemble, Appl. Intell. 51 (3) (2021) 1213–1226.

[18] M. Nishio, S. Noguchi, H. Matsuo, T. Murakami, Automatic classification between COVID-19 pneumonia, non-COVID-19 pneumonia, and the healthy on chest X-ray image: combination of data augmentation methods, Sci. Rep. 10 (1) (2020), https://doi.org/10.1038/s41598-020-74539-2.

[19] A.I. Khan, J.L. Shah, M.M. Bhat, CoroNet: A deep neural network for detection and diagnosis of COVID-19 from chest x-ray images, Comput. Methods Programs Biomed. 196 (2020) 105581.

[20] C. Ouchicha, O. Ammor, M. Meknassi, CVDNet: A novel deep learning architecture for detection of coronavirus (Covid-19) from chest x-ray images, Chaos, Solitons and Fractals. 140 (2020) 110245.

[21] Chest X-ray images (pneumonia). https://www.kaggle.com/paultimothymooney/chest-xray-pneumonia.

[22] J.P. Cohen P. Morrison L. Dao COVID-19 image data collection 2020 https://github.com/ieee8023/covid-chestxray-dataset.

[23] K. He, X. Zhang, S. Ren, J. Sun, Deep residual learning for image recognition, in: Proc. IEEE Comput. Soc. Conf. Comput. Vis. Pattern Recognit., 2016. https://doi.org/10.1109/CVPR.2016.90.

[24] M. Lin, Q. Chen, S. Yan, Network in network, in: 2nd Int. Conf. Learn. Represent. ICLR 2014 - Conf. Track Proc., 2014.

[25] W. Li, K. Liu, L. Yan, F. Cheng, Y.Q. Lv, L.Z. Zhang, FRD-CNN: Object detection based on small-scale convolutional neural networks and feature reuse, Sci. Rep. 9 (1) (2019), https://doi.org/10.1038/s41598-019-52580-0.

[26] G. Huang, Z. Liu, L. Van Der Maaten, K.Q. Weinberger, Densely connected convolutional networks, in: Proc. - 30th IEEE Conf. Comput. Vis. Pattern Recognition, CVPR 2017, 2017. https://doi.org/10.1109/CVPR.2017.243.

[27] K. Simonyan, A. Zisserman, Very deep convolutional networks for large-scale image recognition, in: 3rd Int. Conf. Learn. Represent. ICLR 2015 - Conf. Track Proc., 2015.

[28] N. Noreen, S. Palaniappan, A. Qayyum, I. Ahmad, M. Imran, M. Shoaib, A deep learning model based on concatenation approach for the diagnosis of brain tumor, IEEE Access. 8 (2020) 55135–55144.

[29] Y. Cheng, J. Feng, K. Jia, A Lung Disease Classification Based on Feature Fusion Convolutional Neural Network with X-ray Image Enhancement, in: 2018 Asia-Pacific Signal Inf. Process. Assoc. Annu. Summit Conf. APSIPA ASC 2018 - Proc., 2019. https://doi.org/10.23919/APSIPA.2018.8659700.

[30] W. Hao, S. Zhili, Research on image classification based on improved DenseNet, ACM Int. Conf. Proceeding Ser. (2021), https://doi.org/10.1145/3473714.3473766.

[31] X. Chang, J. Wu, T. Yang, G. Feng, DeepFake Face Image Detection based on Improved VGG Convolutional Neural Network, in: Chinese Control Conf. CCC, 2020. https://doi.org/10.23919/CCC50068.2020.9189596.

[32] J. Luján-García, C. Yáñez-Márquez, Y. Villuendas-Rey, O. Camacho-Nieto, A transfer learning method for pneumonia classification and visualization, Appl. Sci. 10 (8) (2020) 2908.

[33] Y. Sun, A.K.C. Wong, M.S. Kamel, Classification of imbalanced data: A review, Int. J. Pattern Recognit. Artif. Intell. 23 (04) (2009) 687–719.

[34] S. Woo, J. Park, J.Y. Lee, I.S. Kweon, CBAM: Convolutional block attention module, in: Lect. Notes Comput. Sci. (Including Subser. Lect. Notes Artif. Intell. Lect. Notes Bioinformatics), 2018. https://doi.org/10.1007/978-3-030-01234-2_1.

[35] A. He, T. Li, N. Li, K. Wang, H. Fu, CABNet: Category Attention Block for Imbalanced Diabetic Retinopathy Grading, IEEE Trans. Med. Imaging. 40 (1) (2021) 143–153.

[36] D.P. Kingma, J.L. Ba, Adam: A method for stochastic optimization, in: 3rd Int. Conf. Learn. Represent. ICLR 2015 - Conf. Track Proc., 2015.

[37] I. Kandel, M. Castelli, A. Popovič, Comparative study of first order optimizers for image classification using convolutional neural networks on histopathology images, J. Imaging. 6 (9) (2020) 92.

[38] G. Hong, X. Chen, J. Chen, M. Zhang, Y. Ren, X. Zhang, A multi-scale gated multi-head attention depthwise separable CNN model for recognizing COVID-19, Sci. Rep. 11 (1) (2021), https://doi.org/10.1038/s41598-021-97428-8.

[39] P. Chhikara, P. Singh, P. Gupta, T. Bhatia, Deep convolutional neural network with transfer learning for detecting pneumonia on chest x-rays, Adv. Intell. Syst. Comput. (2020), https://doi.org/10.1007/978-981-15-0339-9_13.

[40] O. Stephen, M. Sain, U.J. Maduh, D.-U. Jeong, An efficient deep learning approach to pneumonia classification in healthcare, J. Healthc. Eng. 2019 (2019) 1–7.

[41] S. Wang, J. Sun, I. Mehmood, C. Pan, Y.I. Chen, Y.-D. Zhang, Cerebral micro-bleeding identification based on a nine-layer convolutional neural network with stochastic pooling, Concurr. Comput. Pract. Exp. 32 (1) (2020), https://doi.org/10.1002/cpe.5130.

[42] A.A. Saraiva, N.M. Fonseca Ferreira, L.L. De Sousa, N.C. Costa, J.V.M. Sousa, D.B.S. Santos, A. Valente, S. Soares, Classification of images of childhood pneumonia using convolutional neural networks, in: BIOIMAGING 2019 - 6th Int. Conf. Bioimaging, Proceedings; Part 12th Int. Jt. Conf. Biomed. Eng. Syst. Technol. BIOSTEC 2019, 2019. https://doi.org/10.5220/0007404301120119.

[43] S. Rajaraman, S. Candemir, I. Kim, G. Thoma, S. Antani, Visualization and interpretation of convolutional neural network predictions in detecting pneumonia in pediatric chest radiographs, Appl. Sci. (2018), https://doi.org/10.3390/app8101715.

[44] A. Pant, A. Jain, K.C. Nayak, D. Gandhi, B.G. Prasad, Pneumonia detection: an efficient approach using deep learning, in, 11th Int, Conf. Comput. Commun. Netw. Technol. ICCCNT 2020 (2020) 2020, https://doi.org/10.1109/ICCCNT49239.2020.9225543.

[45] M. Hu, H. Lin, Z. Fan, W. Gao, L. Yang, C. Liu, Q. Song, Learning to recognize chest-xray images faster and more efficiently based on multi-kernel depthwise convolution, IEEE Access. (2020), https://doi.org/10.1109/ACCESS.2020.2974242.
[46] E. Ayan, B. Karabulut, H.M. Ünver, Diagnosis of pediatric pneumonia with ensemble of deep convolutional neural networks in chest x-ray images, Arab. J. Sci. Eng. (2022), https://doi.org/10.1007/s13369-021-06127-z.
[47] S. Heidarian, P. Afshar, N. Enshaei, F. Naderkhani, M.J. Rafiee, F. Babaki Fard, K. Samimi, S.F. Atashzar, A. Oikonomou, K.N. Plataniotis, A. Mohammadi, Covid-fact, A fully-automated capsule network-based framework for identification of COVID-19 cases from chest CT Scans, Front. Artif. Intell. (2021), https://doi.org/10.3389/frai.2021.598932.
[48] M. Alotaibi B. Alotaibi Detection of COVID-19 using deep learning on X-ray images Intell. Autom. Soft Comput. 2021 https://doi.org/10.32604/iasc.2021.018350.
[49] X. Xu, X. Jiang, C. Ma, P. Du, X. Li, S. Lv, L. Yu, Q. Ni, Y. Chen, J. Su, G. Lang, Y. Li, H. Zhao, J. Liu, K. Xu, L. Ruan, J. Sheng, Y. Qiu, W. Wu, T. Liang, L. Li, A deep learning system to screen novel coronavirus disease 2019 pneumonia, Engineering. (2020), https://doi.org/10.1016/j.eng.2020.04.010.
[50] J.E. Luján-García, M.A. Moreno-Ibarra, Y. Villuendas-Rey, C. Yáñez-Márquez, Fast COVID-19 and pneumonia classification using chest X-ray images, Mathematics. (2020), https://doi.org/10.3390/MATH8091423.
[51] A.U. Ibrahim, M. Ozsoz, S. Serte, F. Al-Turjman, P.S. Yakoi, Pneumonia classification using deep learning from chest X-ray images during COVID-19, Cognit. Comput. (2021), https://doi.org/10.1007/s12559-020-09787-5.
[52] Tuberculosis (TB) Chest X-ray Database. https://www.kaggle.com/datasets/tawsifurrahman/tuberculosis-tb-chest-xray-dataset.